




Cite this: DOI: 10.1039/d5ma00476d

# Surface-engineered Ir/Au dendritic catalysts with minimal iridium loading for efficient alkaline oxygen evolution†

Chih-En Tsai, Yi-Ting Wang and Ying-Huang Lai \*

Electrochemical water splitting is a promising strategy for sustainable hydrogen production, yet the sluggish oxygen evolution reaction (OER) at the anode remains a major bottleneck. Here, we report the fabrication of a low-Ir-content electrocatalyst by anchoring sparse Ir atoms onto high-surface-area dendritic gold (Ir/Au-D) via a copper underpotential deposition (UPD) and redox replacement method. Structural characterization confirms the formation of a stable, highly dispersed Ir/Au surface interface without Ir aggregation. Electrocatalytic measurements demonstrate that Ir/Au-D achieves an overpotential of 301 mV at 10 mA cm<sup>-2</sup> in 1.0 M KOH, a low Tafel slope of 36 mV dec<sup>-1</sup>, and a turnover frequency (TOF) of 3.03 s<sup>-1</sup> at 300 mV (vs. 1.23 V), outperforming Pt wire, Ir wire, and bare Au-D electrodes. Stability tests further reveal negligible performance decay over 20 hours of continuous operation. The enhanced OER activity is attributed to the electronic modulation of Ir atoms by the Au substrate and the synergistic effect at the Ir/Au interface, which promotes intermediate formation and product desorption. This hypothesis is experimentally supported by *in situ* surface-enhanced Raman spectroscopy (SERS), which reveals characteristic bands associated with Ir–O and O–O vibrations under applied potentials. This work provides an effective strategy for maximizing catalytic efficiency through minimal noble metal loading and stable interfacial engineering, offering insights for the design of next-generation low-metal-content OER catalysts.

Received 13th May 2025,  
Accepted 7th July 2025

DOI: 10.1039/d5ma00476d

rsc.li/materials-advances

## 1. Introduction

Water splitting is a pivotal process in the development of green energy technologies. When powered by renewable sources such as solar, geothermal, or wind energy, electrochemical water splitting offers a sustainable route for green hydrogen production. In an electrolyzer, electricity drives the decomposition of water into hydrogen and oxygen. However, the sluggish kinetics of the oxygen evolution reaction (OER) at the anode significantly limits the overall efficiency of acidic water splitting systems.<sup>1</sup> The four-electron transfer mechanism involved in OER is substantially slower than the two-electron hydrogen evolution reaction (HER) at the cathode, thus hindering practical applications.<sup>2</sup> Therefore, the development of highly efficient OER catalysts is crucial to advancing water electrolysis technologies.

Iridium-based catalysts are widely regarded as benchmarks for OER, offering high intrinsic activity and remarkable stability

under acidic conditions. The accepted OER mechanism involves the sequential formation of surface intermediates—HO\*, O\*, and HOO\*—during the oxidation of H<sub>2</sub>O to O<sub>2</sub>.<sup>1</sup> The binding strength between these oxygen species and the catalyst surface plays a critical role in determining reaction kinetics. An ideal catalyst should maintain balanced binding energies for HO\*, O\*, and HOO\* to facilitate each step of the OER and avoid over- or under-stabilization of intermediates. Although Ir-based catalysts excel at water dissociation and intermediate adsorption, the final O<sub>2</sub> evolution step remains kinetically hindered. To address this challenge, extensive efforts have been devoted to engineering Ir-based composites through the incorporation of secondary elements to modulate the electronic structure, enhance surface reactivity, and lower the OER overpotential.

The catalytic properties of Ir can be effectively tuned by alloying with secondary elements, creating composites that generate synergistic effects and optimized reaction pathways. Numerous studies have demonstrated that such modifications significantly enhance catalytic performance. For instance, in formic acid oxidation (FAO), PtAu alloy catalysts suppress the indirect reaction pathway, mitigating CO formation and poisoning of Pt nanoparticles.<sup>3,4</sup> In OER systems, NiFe layered double hydroxide (NiFe-LDH) catalysts exhibit high activity by

Department of Chemistry, Tunghai University, Taichung 40704, Taiwan.

E-mail: yhlai@go.thu.edu.tw

† Electronic supplementary information (ESI) available. See DOI: <https://doi.org/10.1039/d5ma00476d>

modulating the electronic structure of Ni through uniformly distributed Fe atoms, facilitating the adsorption and conversion of key intermediates such as  $^*\text{OOH}$ .<sup>5</sup> Similarly, PtNi bimetallic nanoparticles display excellent HER activity under acidic conditions, with Ni adjusting the d-band structure of Pt to optimize hydrogen adsorption and reaction kinetics while preventing site poisoning.<sup>6</sup> Collectively, these examples underscore the effectiveness of strategic secondary element incorporation in tailoring catalytic activity and stability.

Effective catalyst design must aim to minimize energy barriers across the entire reaction coordinate, from reactant adsorption and bond cleavage to product formation and desorption. In the context of OER, IrAu alloy catalysts have shown enhanced activity, attributed to the formation of distinct Au/Ir interfacial sites.<sup>7</sup> The incorporation of Au, with its lower oxygen affinity, facilitates tandem catalysis with Ir and promotes OER activity. Moreover, the inherent immiscibility between Au and Ir over a wide compositional and temperature range favors the formation of phase-separated structures, preserving active interfaces that contribute to improved catalytic performance and durability.<sup>7,8</sup> In addition, the unique properties of gold nanostructures can further benefit catalyst design. For example, their surface plasmon resonance (SPR) effect enables *in situ* surface-enhanced Raman spectroscopy (SERS) for monitoring reaction mechanisms.<sup>9,10</sup> Three-dimensional architectures based on Au can also serve as robust and conductive supports.<sup>11</sup> Furthermore, gold nanostructures hold potential for light-enhanced catalysis, adding another functional dimension to their role in electrocatalytic systems.<sup>12</sup>

While constructing heterometallic interfaces effectively accelerates OER kinetics, achieving high overall reaction rates ultimately depends on maximizing the density of active sites. The turnover frequency (TOF)—defined as the number of catalytic events per active site per second—serves as a critical metric of intrinsic catalytic efficiency. Low metal content electrocatalysts (LMCEs) have recently attracted attention, demonstrating high TOF values despite minimal noble metal usage.<sup>13</sup> Representative LMCEs, such as AuIr/C ( $0.6\text{ s}^{-1}$ ),  $\text{Co}_3\text{O}_4$  ( $1.07\text{ s}^{-1}$ ), and commercial  $\text{IrO}_2$  ( $0.87\text{ s}^{-1}$ ), achieve remarkable performance at overpotentials of around  $0.3\text{ V}$ .<sup>14,15</sup> Some advanced systems have even reported TOF values up to  $2.2\text{ s}^{-1}$  at  $0.3\text{ V}$  (vs.  $1.23\text{ V}$ ).<sup>16</sup> Nevertheless, conventional Ir alloys and core-shell structures often face challenges in fully utilizing active sites, whereas surface alloying on dendritic Au offers a promising strategy for maximizing interfacial exposure.

Building upon the superior performance of IrAu alloys, this study proposes the fabrication of high-surface-area dendritic gold (Au-D) substrates, onto which a sparse amount of Ir is deposited *via* low-potential copper underpotential deposition followed by redox replacement. This approach aims to create a high-density Ir-modified surface alloy (Ir/Au-D) with maximized active site exposure. The OER performance of these surface-engineered catalysts, featuring isolated Ir atoms anchored on a dendritic gold framework, is systematically investigated.

## 2. Experimental section

### 2.1. Materials and chemicals

Hexachloroiridic acid hydrate ( $\text{H}_2\text{IrCl}_6 \cdot x\text{H}_2\text{O}$ , 95–97%) and sulfuric acid ( $\text{H}_2\text{SO}_4$ , 95–97%) were obtained from Sigma-Aldrich. Tetrachloroauric acid ( $\text{HAuCl}_4$ , 99.9%) was purchased from Alfa Aesar. Copper(II) sulfate pentahydrate ( $\text{CuSO}_4 \cdot 5\text{H}_2\text{O}$ ) and potassium hydroxide (KOH) were acquired from Merck. Platinum and iridium wires (0.5 mm diameter) were obtained from MaTecK. Carbon fiber paper (CFP) supplied by CeTech Co., Ltd. was used as the substrate for catalyst deposition. All chemicals were used as received without further purification. Deionized water was used throughout all experimental procedures.

### 2.2. Material characterization

Electrodeposition was conducted using a conventional three-electrode setup connected to an electrochemical workstation (CHI 611E). A saturated calomel electrode (SCE) was used as the reference electrode, and a carbon rod served as the counter electrode. Powder X-ray diffraction (XRD) patterns were obtained at the BL23A SWAXS end station and TPS 13A end station of the National Synchrotron Radiation Research Center (NSRRC, Taiwan) using monochromatic X-rays with a wavelength of  $0.827\text{ \AA}$  ( $15\text{ keV}$ ).<sup>17,18</sup> Data were collected on an image plate, and the diffraction angle ( $2\theta$ ) was calibrated using a mixed powder standard of silicon and silver behenate. X-ray photoelectron spectroscopy (XPS) measurements were performed at the photoelectron spectroscopy (PES) end station of beamline 24A1 at NSRRC. The Fermi level was calibrated using the photoemission onset from a gold foil mounted on the sample holder. Au and Ir XPS spectra of the Ir/Au-D catalysts were acquired using an incident photon energy of  $530\text{ eV}$ . Thermogravimetric analysis (TGA) was conducted using a Mettler Toledo TGA/DSC 2 instrument. Field-emission scanning electron microscopy (FE-SEM) images were acquired using a JEOL JEM-2100F microscope operated at an accelerating voltage of  $5.0\text{ kV}$ . The elemental composition and atomic ratios of Ir and Au were quantified by inductively coupled plasma mass spectrometry (ICP-MS, Thermo X Series II). Transmission electron microscopy (TEM) and energy-dispersive X-ray spectroscopy (EDS) mapping of the catalyst samples were performed on a Talos F200X G2 field emission scanning transmission electron microscope. The Ir/Au-D experiments were conducted in an *in situ* Raman electrochemical cell using a CHI 611E potentiostat. Raman spectra were recorded using a micro-Raman system equipped with a  $632.8\text{ nm}$  laser and a  $100\times$  objective lens (NA 0.65, Olympus). For each applied potential, the spectral acquisition time was 20 seconds.<sup>19,20</sup>

### 2.3. Electrochemical measurements

The oxygen evolution reaction (OER) activity and long-term durability of the catalysts were evaluated using a conventional three-electrode H-type cell. The working electrodes consisted of catalyst-coated carbon fiber paper (CFP) substrates with a geometric area of  $1 \times 1\text{ cm}^2$ . A saturated calomel electrode



(SCE) and a carbon rod were used as the reference and counter electrodes, respectively. All electrochemical measurements were conducted in 1.0 M KOH or 0.5 M H<sub>2</sub>SO<sub>4</sub> electrolytes. Linear sweep voltammetry (LSV) was performed at a scan rate of 10 mV s<sup>-1</sup> with full iR compensation. All measured potentials were converted to the reversible hydrogen electrode (RHE) scale using the following equation:

$$E_{\text{RHE}} = E_{\text{SCE}} + 0.245 \text{ V} + 0.059 \times \text{pH}.$$

The Tafel slopes were determined by fitting the LSV data to the Tafel equation:  $\eta = b \log j + c$ , where  $\eta$  is the overpotential,  $b$  is the Tafel slope,  $j$  is the current density, and  $c$  is the intercept. The exchange current density ( $j_0$ ) was calculated using the relation:  $j_0 = 10^{-c/b}$ .

#### 2.4. Fabrication of Ir/Au-D catalysts

The preparation method for Ir/Au-D catalysts is illustrated in Fig. 1. Dendritic gold structures (Au-D) were first synthesized using a pulsed electrochemical deposition technique.<sup>19</sup> A three-electrode system was employed, consisting of a carbon fiber paper (CFP) working electrode (geometric area: 1 × 1 cm<sup>2</sup>), a saturated calomel electrode (SCE) as the reference, and a carbon rod as the counter electrode. The electrolyte contained 0.5 M H<sub>2</sub>SO<sub>4</sub> supplemented with 0.10 mM cysteine and 1 mM HAuCl<sub>4</sub>. Pulsed potentials ranging from 0 to -0.8 V (vs. SCE) were applied with a step time of 0.1 s for 30 000 cycles. After deposition, the Au-D samples were rinsed thoroughly with deionized water.

Cysteine molecules adsorbed on the Au-D surface were subsequently removed under alkaline conditions. Following surface purification, copper atoms were deposited onto the Au-D substrate at low potentials through underpotential deposition (UPD).<sup>12</sup> Finally, a spontaneous redox replacement reaction was conducted to substitute the deposited Cu atoms with Ir atoms, forming an Ir-modified Au surface alloy (Ir/Au-D).<sup>21,22</sup> Specifically, the electrodes were immersed in a 5.0 mM aqueous solution of potassium hexachloroiridate (K<sub>2</sub>IrCl<sub>6</sub>) for 10 minutes to complete the Ir deposition.

### 3. Result and discussion

#### 3.1. Characterization of Au-D and Ir/Au-D

To confirm the successful Ir modification at low loading, the Ir/Au-D electrodes were further oxidized to form IrO<sub>2</sub>/Au-D under

alkaline conditions. Electrochemical characterization was performed based on the distinct and stable redox features of gold observed in acidic cyclic voltammetry (CV) profiles.<sup>12,23</sup> CV measurements were carried out in 0.5 M H<sub>2</sub>SO<sub>4</sub> within a potential range of -0.13 to 1.83 V (vs. RHE) at a scan rate of 10 mV s<sup>-1</sup>, as shown in Fig. 2(A).

The CV profile of Au-D (black line) exhibited a prominent oxidation peak between 1.35 and 1.65 V (vs. RHE), corresponding to the oxidation of gold.<sup>24</sup> The dendritic structure of Au-D exposed a high density of high-index crystal facets, such as (311), alongside low-index planes including (111), (100), and (110), resulting in a substantially enlarged electrochemically active surface area (ECSA).<sup>25</sup> The ECSA was estimated based on the reduction peak at 1.10 V (vs. RHE), assuming a surface charge density of 386 μC cm<sup>-2</sup>. The calculated ECSA revealed that each 1 × 1 cm<sup>2</sup> CFP electrode coated with Au-D exhibited approximately 81.8 cm<sup>2</sup> of active surface area, corresponding to an ~80-fold enhancement relative to the geometric area.

During electrode fabrication, cysteine molecules with sulfur functional groups formed Au-S bonds with the gold surface, directing preferential growth along the (111) planes and promoting the formation of the dendritic nanostructure.<sup>11</sup> Cysteine desorption was subsequently achieved by reductive treatment in 0.50 M KOH within a potential window of -0.4 to 1.6 V (vs. SCE).

Following surface cleaning, copper UPD was performed onto the dendritic Au surface, with the suitable potential window identified in Fig. 2(B). Significant copper deposition occurred at potentials more negative than -0.32 V. To ensure selective Ir replacement, UPD of Cu was conducted at -0.28 V (vs. SCE) in this study. After forming a submonolayer of Cu atoms, the electrodes were immersed in a 5 mM Ir<sup>4+</sup> solution, triggering a spontaneous redox replacement reaction. Based on standard reduction potentials (Cu<sup>2+</sup>: +0.34 V < Ir<sup>4+</sup>: +0.87 V < Au<sup>3+</sup>: +0.93 V vs. SHE), Ir<sup>4+</sup> ions thermodynamically favor the reduction by Cu atoms, consuming two Cu atoms for the incorporation of one Ir atom.

Upon successful Ir deposition, notable changes were observed in the CV profiles (orange line, Fig. 2A). A significant decrease in the oxidation peak at ~1.40 V indicated the coverage of incompletely coordinated or highly reactive gold sites by Ir. Meanwhile, the Au reduction peak slightly shifted to +1.13 V with reduced intensity, yielding a final ECSA of approximately 65.6 cm<sup>2</sup>. Compared to the initial ECSA of 81.8 cm<sup>2</sup>, this reduction reflects the surface coverage of dendritic tips and

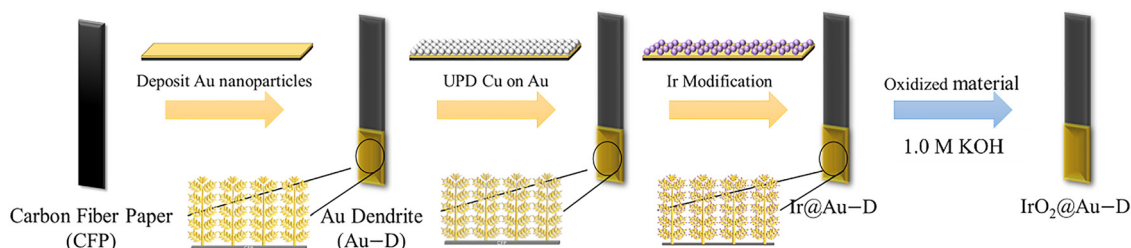


Fig. 1 Schematic illustration of the fabrication process for three-dimensional dendritic gold (Au-D), Ir/Au-D, and IrO<sub>2</sub>/Au-D catalysts.



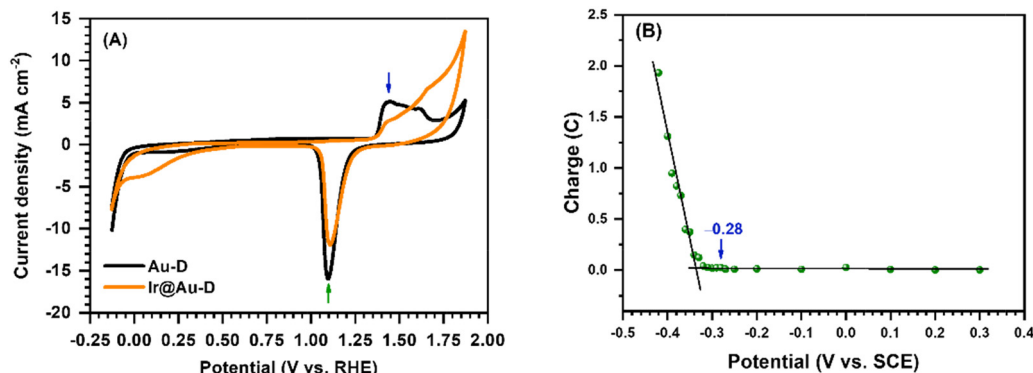


Fig. 2 (A) Cyclic voltammograms (CVs) of Au-D (black line) and Ir@Au-D (orange line) recorded in 0.5 M  $\text{H}_2\text{SO}_4$  at a scan rate of  $10 \text{ mV s}^{-1}$ . (B) Plot of charge versus potential during Cu underpotential deposition (UPD); the applied potential is referenced to the SCE electrode used in the actual experiment.

high-curvature regions by Ir atoms, resulting in a smoother overall morphology.

### 3.2. Structural and morphological characterization

The morphological evolution of Au-D, Ir/Au-D, and  $\text{IrO}_2/\text{Au-D}$  was investigated using scanning electron microscopy (SEM), as shown in Fig. 3. The SEM images of the electrochemically synthesized Au-D (Fig. 3A and B) reveal a distinct three-dimensional dendritic architecture, with primary trunks extending several hundred micrometers and secondary branches of similar lengths. Numerous nanoscale protrusions ( $\sim$ hundreds of nanometers) were observed along the branches. The structure featured abundant sharp tips and high-curvature edges, offering a large specific surface area favorable for catalytic applications. The chemical stability of gold across a wide pH range further supports its use as a robust support for catalyst integration.

Following copper UPD, Ir redox replacement, and surface modification, the SEM image of Ir/Au-D (Fig. 3C) shows that the dendritic morphology remained largely intact. However, slight blunting of the high-curvature regions was observed, consistent with the previously noted reduction in electrochemically active surface area (ECSA). The conservative UPD potential ( $-0.28 \text{ V vs. SCE}$ ) ensured sub-monolayer deposition of copper, of which only half could be replaced by Ir. Therefore, the actual Ir loading was even lower than that of the Cu sub-monolayer. This was further validated by inductively coupled plasma mass spectrometry (ICP-MS). Notably, no Ir nanoparticles were visible on the surface in SEM images, indicating that Ir atoms were atomically dispersed without aggregation. After oxidation under alkaline conditions, the  $\text{IrO}_2/\text{Au-D}$  sample (Fig. 3D) maintained its dendritic structure, though further surface smoothing at the tips and edges was observed. This result suggests that the 3D framework remained structurally stable after Ir oxidation.

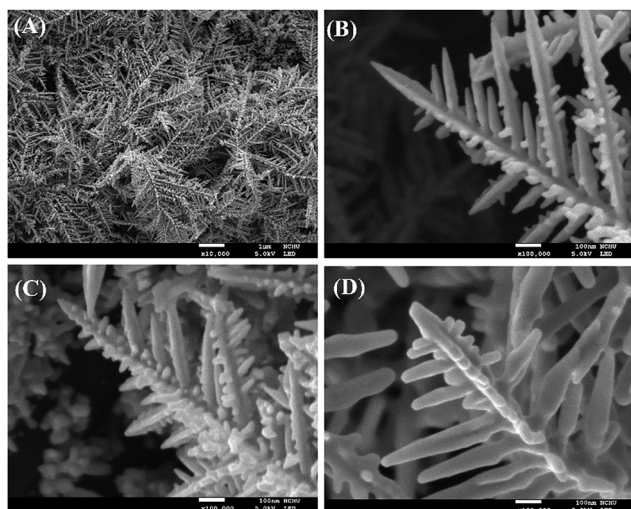


Fig. 3 (A) Low-magnification SEM image showing the large-scale three-dimensional morphology of dendritic Au-D. (B) Higher magnification SEM image of Au-D highlighting its branched structure. (C) SEM image of Ir-modified dendritic gold (Ir/Au-D). (D) SEM image of oxidized  $\text{IrO}_2/\text{Au-D}$  after alkaline treatment.

### 3.3. Nanoscale characterization of Ir distribution by TEM and EDS

To further investigate the nanostructural features, Ir/Au-D samples detached from the CFP substrate were analyzed by transmission electron microscopy (TEM) and energy-dispersive X-ray spectroscopy (EDS), as shown in Fig. 4. The TEM image (Fig. 4A) confirms that the three-dimensional dendritic framework of Au-D was preserved even after Ir modification. Although slight surface smoothing occurred during sample preparation, no aggregation of Ir nanoparticles was observed, suggesting that Ir atoms were highly dispersed or formed ultra-small clusters. This atomic-level dispersion maximizes Ir atom utilization and contributes to the catalyst's enhanced oxygen evolution reaction (OER) performance.

EDS elemental mapping (Fig. 4B–F) further supports the presence and distribution of Ir across the Au-D surface. While the Ir signal appears relatively uniform without obvious localized enrichment, we acknowledge that the spatial resolution of conventional EDS is insufficient to confirm atomic-scale dispersion. Moreover, the sample preparation involved a





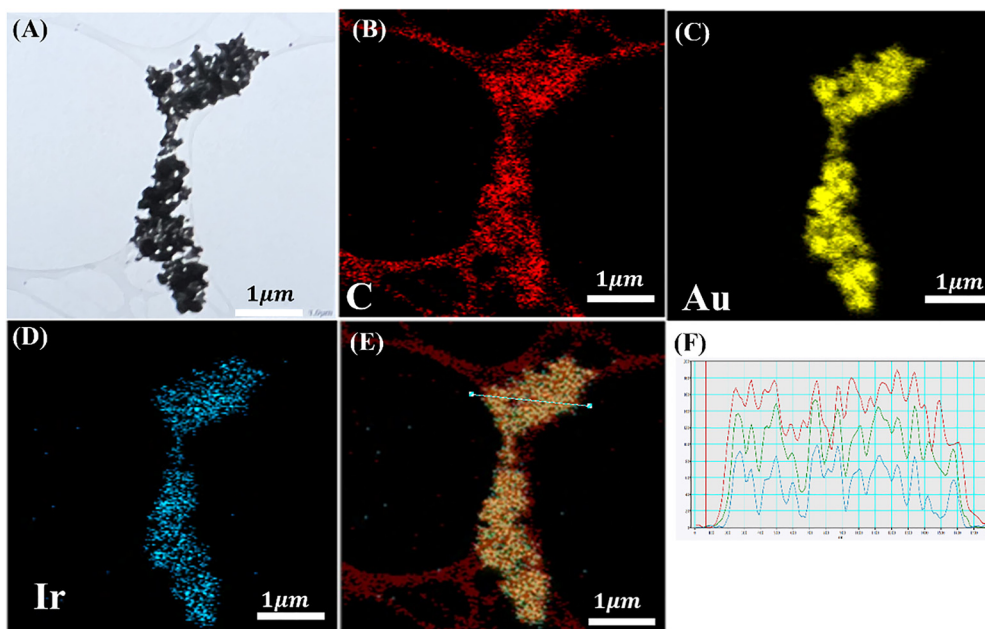


Fig. 4 Transmission electron microscopy (TEM) and energy-dispersive X-ray spectroscopy (EDS) analysis of Ir/Au-D detached from the CFP electrode. (A) TEM image of Ir/Au-D. (B)–(D) EDS elemental maps showing the distribution of (B) carbon (C), (C) gold (Au), and (D) iridium (Ir). (E) Overlay of EDS maps illustrating the spatial distribution of C, Au, and Ir. (F) EDS line-scan profile of Ir/Au-D from (E), with red representing C, green for Au, and blue for Ir.

wet-transfer process, during which the Ir/Au-D catalyst was detached from the CFP substrate and deposited onto a copper grid with a carbon support film. This process may have introduced contrast artifacts or minor aggregation that artificially enhance Ir visibility in Fig. 4(E). Therefore, although SEM and XRD show no evidence of Ir nanoparticles or crystalline clusters, confirming true atomic-level dispersion would require higher-resolution techniques such as aberration-corrected STEM or X-ray absorption spectroscopy (XAS), which are planned for future investigation.

### 3.4. Crystallographic analysis by XRD

The crystalline structures of Au-D and Ir/Au-D were examined by X-ray diffraction (XRD), as shown in Fig. 5. The XRD pattern of Au-D (red line) displays five characteristic peaks at  $38.2^\circ$ ,  $44.4^\circ$ ,  $64.6^\circ$ ,  $77.6^\circ$ , and  $81.7^\circ$ , corresponding to the (111), (200), (220), (311), and (222) planes of face-centered cubic (FCC) gold, respectively (JCPDS no. 04-0784). The strongest intensity was observed for the (111) reflection, and the intensity ratio  $I_{(111)}/I_{(200)}$  exceeded 3.0, indicating a strong (111) texture. This suggests preferential growth along the (111) plane and a highly branched structure driven by the low surface energy of the FCC lattice during electrochemical deposition.<sup>23,26</sup>

The XRD pattern of Ir/Au-D (orange line) retained all major Au reflections with similar peak positions and relative intensities after Ir deposition. No additional peaks associated with Ir or its oxides were observed, likely due to the extremely low Ir loading and the absence of large Ir crystallites. Even if surface alloying or small Ir clusters were present, their concentration was insufficient to produce detectable diffraction signals. Furthermore, due to the limited miscibility between Au and Ir

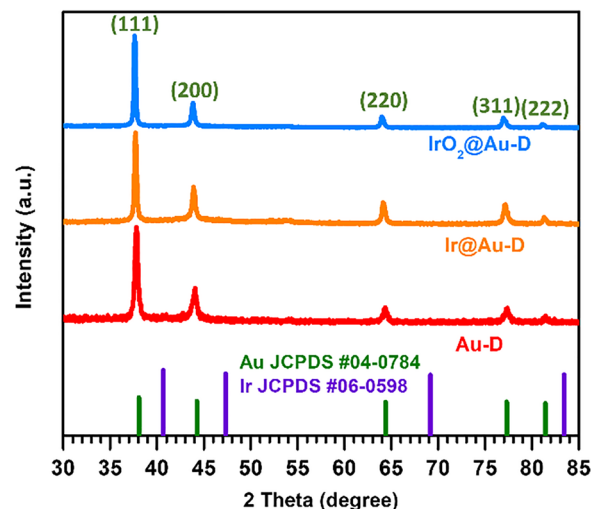


Fig. 5 X-ray diffraction (XRD) patterns of Au-D, Ir/Au-D, and IrO<sub>2</sub>/Au-D. Reference diffraction data are based on Au (JCPDS #04-0784) and Ir (JCPDS #06-0598).

across broad compositional and temperature ranges,<sup>7,8</sup> Ir atoms did not diffuse into the Au lattice but remained on the surface in a phase-separated state. This configuration is favorable for generating abundant and accessible Ir/Au interfacial sites that support enhanced catalytic activity.

### 3.5. Surface chemical composition and oxidation states

To investigate the surface chemical states and composition of Ir/Au-D and IrO<sub>2</sub>/Au-D, X-ray photoelectron spectroscopy (XPS) measurements were conducted. High-resolution spectra of Au 4f and Ir 4f regions are shown in Fig. 6(A) and (B), respectively.



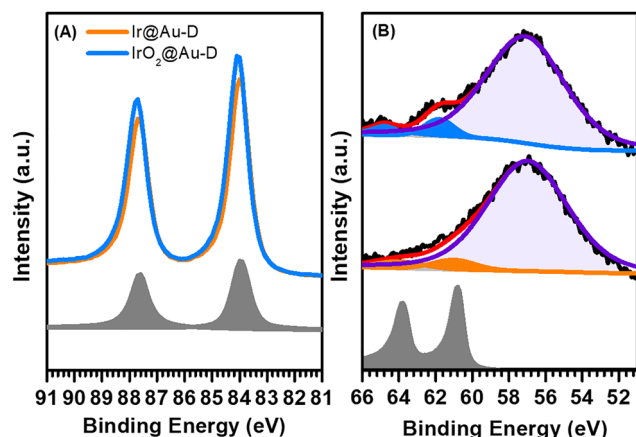


Fig. 6 X-ray photoelectron spectroscopy (XPS) analysis: (A) Au 4f spectra of Au-D (gray), Ir/Au-D (orange), and IrO<sub>2</sub>/Au-D (blue). (B) Ir 4f and Au 5p spectra of Ir wire (gray), Ir/Au-D (orange), and IrO<sub>2</sub>/Au-D (blue).

For Au-D (gray line, Fig. 6A), the Au 4f<sub>7/2</sub> and Au 4f<sub>5/2</sub> peaks were located at 84.0 eV and 87.6 eV, respectively, consistent with metallic Au in a standard reference foil. After Ir deposition (orange line), no shift in Au 4f binding energy was observed, and the peak separation remained 3.6 eV. This indicates that the introduction of Ir had minimal influence on the local chemical environment of Au, consistent with the metallic state of Ir deposited *via* redox replacement.

Following oxidative treatment in alkaline solution, Ir/Au-D was converted into IrO<sub>2</sub>/Au-D. A slight positive shift in the Au 4f binding energies was observed (to 84.1 eV and 87.7 eV), accompanied by an increase in full width at half maximum (FWHM) from 0.9 to 1.0 eV. This suggests a minor alteration in the electronic environment of Au due to surface Ir oxidation, while confirming that Au itself remained unoxidized—consistent with a phase-separated Au–Ir structure.

The Ir 4f<sub>7/2</sub> signal for standard metallic Ir foil appeared at 61.6 eV (gray line, Fig. 6B), representing Ir<sup>0</sup>. In Ir/Au-D, however, the Ir 4f signal overlapped with the Au 5p peak, making direct identification difficult due to the extremely low Ir loading. To resolve this, the Ir atoms were oxidized under alkaline conditions, yielding IrO<sub>2</sub>/Au-D. After oxidation, a distinct Ir 4f<sub>7/2</sub> peak emerged at 62.3 eV (blue line, Fig. 6B), corresponding to Ir<sup>4+</sup> species.<sup>27,28</sup> This confirms that the surface Ir atoms were successfully oxidized into IrO<sub>2</sub>, a well-known OER-active phase.<sup>29</sup>

The XPS results support that Ir was atomically dispersed across the Au-D surface and retained in a phase-separated form, both before and after oxidation. The generation of IrO<sub>2</sub> at the interface during OER provides abundant, stable, and catalytically active Ir<sup>4+</sup> sites, enhancing oxygen evolution efficiency.

### 3.6. Electrochemical performance and kinetics

The OER activity of the catalysts was evaluated in 1.0 M KOH using a three-electrode H-cell setup. Linear sweep voltammetry

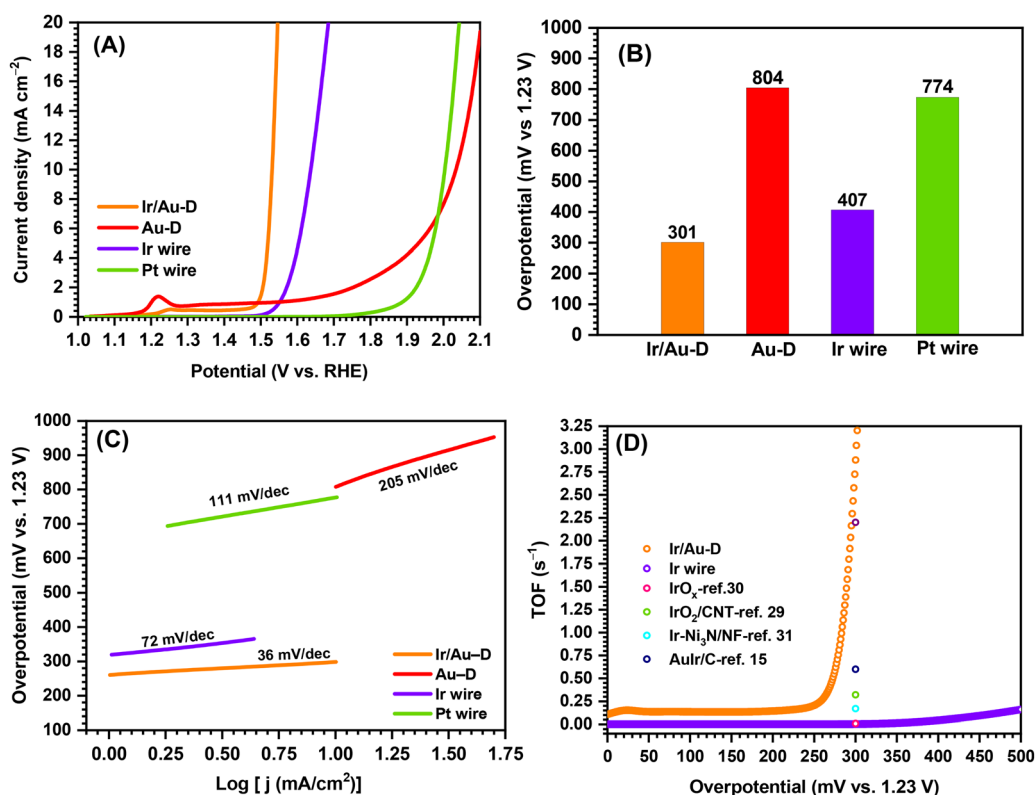


Fig. 7 OER performance of Pt wire, Ir wire, Au-D, and Ir/Au-D in 1.0 M KOH: (A) linear sweep voltammetry (LSV) curves recorded at a scan rate of 10 mV s<sup>-1</sup> with iR compensation. (B) Comparison of overpotentials ( $\eta_{10}$ ) at 10 mA cm<sup>-2</sup>. (C) Tafel plots of the four catalysts. (D) Turnover frequencies (TOFs) of Ir/Au-D and Ir wire, benchmarked against IrO<sub>x</sub>, IrO<sub>2</sub>/CNT, IrNi<sub>3</sub>N/NF, and Aulr/C at an overpotential of 300 mV (vs. 1.23 V).<sup>15,30–32</sup>



(LSV) curves were obtained for Au-D, Ir/Au-D, Pt wire, and Ir wire (Fig. 7A). All tested electrodes exhibited OER activity, but with distinct performance levels. Measurements were performed at a scan rate of 10 mV s<sup>-1</sup> with 90% iR compensation.

Au-D (red line) showed an oxidation peak near 1.22 V (vs. RHE), followed by a gradual increase in current density. The overpotential required to reach 10 mA cm<sup>-2</sup> ( $\eta_{10}$ ) was 804 mV. Pt wire (green) showed  $\eta_{10}$  at 774 mV, while Ir wire (purple) displayed significantly better performance with  $\eta_{10}$  of 407 mV. As expected, Ir exhibited the best intrinsic activity among the pure metals, in agreement with previous studies.

Remarkably, Ir/Au-D outperformed all reference electrodes with an  $\eta_{10}$  of only 301 mV (vs. 1.23 V). After Ir decoration, the oxidation peak of Au diminished, suggesting partial surface coverage by Ir atoms. Fig. 7(B) summarizes  $\eta_{10}$  values, confirming the superior performance of Ir/Au-D, which also compares favorably with top-performing Ir-based catalysts reported in literature.

The enhanced OER activity is attributed to the formation of abundant Ir/Au interfacial sites, where OH<sup>-</sup> ions can interact effectively.<sup>29</sup> The dendritic Au framework modulates the local electronic structure of Ir, particularly near low-coordination sites, where the higher electronegativity of Au induces partial electron withdrawal from Ir. This electronic modulation stabilizes the Ir<sup>4+</sup> oxidation state, which facilitates O-O bond formation and reduces overpotential.

### 3.7. Tafel slope analysis and kinetic evaluation

The Tafel slope, a kinetic parameter for assessing electrocatalytic reaction mechanisms, is presented in Fig. 7(C). The slopes for Au-D, Pt wire, Ir wire, and Ir/Au-D were measured as 205, 111, 72, and 36 mV dec<sup>-1</sup>, respectively. The elevated slope for Au-D is attributed to additional contributions from Au oxidation at relevant current densities. Ir/Au-D exhibits the smallest Tafel slope, indicating rapid kinetics and efficient charge transfer, with performance surpassing even that of bulk Ir wire (72 mV dec<sup>-1</sup>), consistent with literature values for Ir catalysts (~70 mV dec<sup>-1</sup>). These results confirm that the Ir/Au interface effectively lowers the energy barrier for oxygen evolution, enabling rapid increases in current density with only minor

overpotential increments. The superior kinetics and low onset potential position Ir/Au-D as a highly efficient OER catalyst.

### 3.8. Turnover frequency (TOF) and catalyst utilization

The intrinsic activity of Ir/Au-D was further assessed by calculating the turnover frequency (TOF), which correlates catalyst loading with reaction rate.<sup>2</sup> ICP-MS analysis determined the metal content as 0.182 ppm Ir and 73.48 ppm Au. Combined with TGA, the residual metal mass per electrode was 0.66 mg Au and 1.59  $\mu$ g Ir, corresponding to  $2.03 \times 10^{18}$  Au atoms and  $5.15 \times 10^{15}$  Ir atoms per cm<sup>2</sup>. This low Ir content aligns with the definition of a low-metal-content electrocatalyst (LMCE). Assuming a uniform monolayer distribution and an FCC (111) atom density of  $7.83 \times 10^{14}$  atoms cm<sup>-2</sup>, the surface coverage by Ir was estimated at 6.6 cm<sup>2</sup>—representing 8.1% of the Au ECSA (81.8 cm<sup>2</sup>). At an overpotential of 300 mV (vs. 1.23 V), the TOF of Ir/Au-D was calculated to be 3.03 s<sup>-1</sup> ( $1.56 \times 10^{16}$  O<sub>2</sub> molecules s<sup>-1</sup>  $\div$   $5.15 \times 10^{15}$  Ir atoms). Fig. 7(D) displays the TOF-potential profile. When compared to other Ir-based catalysts tested at the same overpotential, Ir/Au-D demonstrated one of the highest TOF values reported to date.<sup>15,30–32</sup> This outstanding performance arises from the highly dispersed Ir atoms forming a dense population of catalytically active Ir/Au interfacial sites. The dendritic Au scaffold not only stabilizes these sites but also facilitates intermediate formation and product desorption, resulting in enhanced overall catalytic efficiency.

Table 1 summarizes the key performance metrics of various Au–Ir-based catalysts toward the oxygen evolution reaction (OER), highlighting differences in structural design, electrolyte conditions, and electrochemical performance. Among the listed systems, Ir/Au-D, synthesized in this work, demonstrates excellent OER activity with a low overpotential of 301 mV at 10 mA cm<sup>-2</sup> in 1.0 M KOH, a Tafel slope of 36 mV dec<sup>-1</sup>, and a high turnover frequency (TOF) of 3.03 s<sup>-1</sup> at 300 mV, which surpasses most reported analogs under comparable or acidic conditions. Compared to core-shell or alloy structures such as Au–Ir nanostars or Au–Ir alloy nanoparticles,<sup>7,30,31</sup> the atomically dispersed Ir species anchored on the dendritic Au framework offer a significantly higher surface-normalized activity and robust long-term stability (over 20 hours). In contrast,

**Table 1** Performance metrics of Au–Ir-based catalysts for OER: overpotential, Tafel slope, and durability

Catalyst (system)	Electrolyte	Overpotential@ 10 mA cm <sup>-2</sup> (mV)	Tafel slope (mV dec <sup>-1</sup> )	TOF (s <sup>-1</sup> )	Stability	Key features	Ref.
Ir/Au-D	1.0 M KOH	301	36	3.03 (@300 mV)	>20 h stable	Dendritic Au with atomically dispersed Ir	This work
Ir@Au core-shell NPs	0.1 M HClO <sub>4</sub>	310	42	—	10 h	Ir-rich shell over Au core	30
Au–Ir nanostars	0.1 M HClO <sub>4</sub>	~285	~36	—	12 h	Abundant active sites due to branched morphology	7
Ir-doped Au-LDH	1.0 M KOH	~320	~45	1.2 (@300 mV)	10 h	Layered double hydroxide structure	32
Au–Ir/C (UPD-redox method)	0.1 M HClO <sub>4</sub>	270	36	—	20 h	UPD-based quasi-single-atom interface	15
Au@IrO <sub>x</sub> (electrodeposited)	0.1 M HClO <sub>4</sub>	340	~60	—	6 h	Strong Ir–Au interaction suppresses Ir leaching	33
Pt/C (commercial)	0.1 M HClO <sub>4</sub>	~540	~67	—	—		34



some systems, such as Au/IrO<sub>x</sub> or Ir–Au alloy films, suffer from shorter durability ( $\leq 12$  h), partly due to structural or interfacial instability under acidic OER conditions.<sup>33</sup> Notably, the layered double hydroxide (LDH)-type Ir-doped Au and UPD-redox fabricated quasi-single-atom systems show competitive overpotentials (270–320 mV) and stability ( $\sim 10$ –20 h), but generally lack TOF values or detailed surface metrics, which limits direct kinetic comparisons.<sup>15,32,33</sup>

Importantly, when benchmarked against the most commonly used Pt/C catalyst, Ir/Au-D still outperforms in every key metric. Commercial Pt/C requires an overpotential of  $\approx 400$  mV to reach  $10 \text{ mA cm}^{-2}$  in 1.0 M KOH and exhibits a Tafel slope of  $\approx 70 \text{ mV dec}^{-1}$ , with stability typically limited to under 2 h due to Pt dissolution and restructuring.<sup>34</sup> Even in acidic media (0.1 M HClO<sub>4</sub>), Pt/C shows an overpotential exceeding 520 mV and rapid performance decay within 3 h. Thus, Ir/Au-D achieves a uniquely favorable balance of low overpotential, fast reaction kinetics, and excellent durability in alkaline media. These advantages stem from the synergistic combination of dendritic Au morphology (high-index facets, abundant tips) and the uniform dispersion of isolated Ir atoms, which maximizes active-site exposure while suppressing Ir agglomeration or leaching. This positions Ir/Au-D as a leading design among Au–Ir-based electrocatalysts and a superior alternative to conventional Pt/C for efficient and stable OER operation.

### 3.9. Long-term stability

The long-term durability of Ir/Au-D under OER conditions was assessed *via* a constant-current chronopotentiometry test conducted in 1.0 M KOH. As shown in Fig. 8, the catalyst was operated at a fixed current density of  $10 \text{ mA cm}^{-2}$  for nearly 20 hours, during which the applied potential remained remarkably stable. This result demonstrates that the atomically dispersed Ir species on the dendritic Au framework formed robust and persistent Au–Ir interfacial sites that maintained high catalytic activity over prolonged operation. The excellent

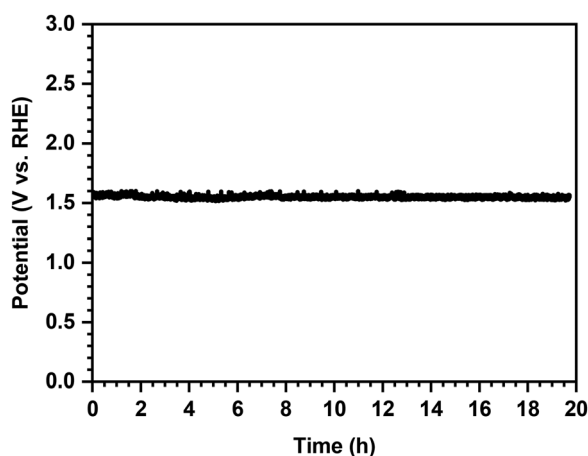


Fig. 8 Chronopotentiometric stability test of Ir/Au-D in 1.0 M KOH at a constant current density of  $10 \text{ mA cm}^{-2}$ .

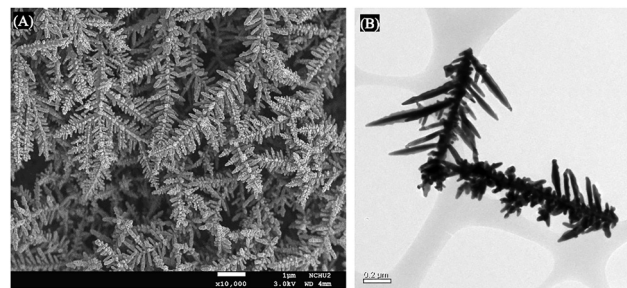


Fig. 9 (A) SEM and (B) TEM images of Ir/Au-D after 20-hour stability testing.

electrochemical stability confirms the structural integrity of the Ir/Au-D system under continuous alkaline OER conditions, Fig. 9.

### 3.10. *In situ* surface-enhanced Raman spectroscopy (SERS) analysis of OER on Ir/Au-D

Au-D exhibits a strong surface plasmon resonance (SPR) effect, making it an excellent SERS substrate.<sup>19</sup> By performing OER on Ir/Au-D, we can use *in situ* SERS to track changes in the surface IrO<sub>2</sub> species. Fig. 10 shows the *in situ* SERS spectra collected in 1.0 M KOH under various applied potentials: (a) open-circuit potential (OCP) before reaction, (b)  $-0.27 \text{ V}$  (vs. 1.23V) (c)  $-0.30 \text{ V}$  and (d) OCP again after completing the OER. At OCP

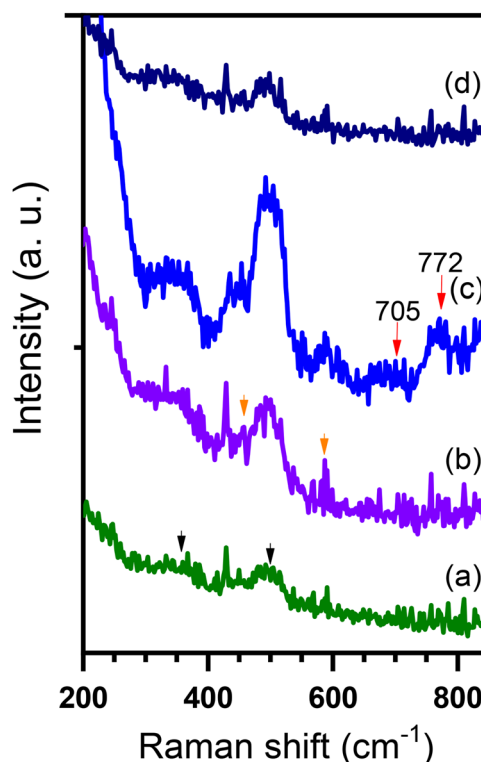


Fig. 10 *In situ* SERS spectra of Ir/Au-D during OER: (a) at open circuit potential (OCP), (b) at  $-0.27 \text{ V}$ , (c) at  $-0.30 \text{ V}$ , and (d) after the reaction (OCP). The spectrum for each potential condition represents the average of 20 scans.





(Fig. 10a), the Raman spectrum of Ir/Au-D displays two broad peaks at 340 and 502  $\text{cm}^{-1}$ , which correspond to the twist and stretching modes of Ir–O–Ir in  $\text{Ir}^{4+}$  oxide.<sup>35</sup> When  $-0.27$  V is applied, gas bubbles begin to form at the electrode surface, and the SERS spectrum (Fig. 10b) shows increased intensity at 470 and 590  $\text{cm}^{-1}$ . These bands are attributed to  $\mu$ -oxo-type Ir–O–Ir stretching vibrations arising from the basal planes of edge-sharing  $\text{IrO}_6$  octahedra.<sup>36</sup> At  $-0.30$  V (Fig. 10c), two additional features appear: a weak band at 705  $\text{cm}^{-1}$  assigned to O–O stretching and a stronger band at 772  $\text{cm}^{-1}$  assigned to Ir–O stretching at square-pyramidal Ir sites.<sup>36</sup> These results indicate that the active centers for the OER on Ir/Au-D are indeed the Ir atoms. After the OER test, returning the potential to OCP restores the SERS spectrum (Fig. 10d) to one closely matching the pre-reaction state, with all intermediate-state signals disappearing.

## 4. Conclusion

In this work, a surface alloy electrocatalyst (Ir/Au-D) was successfully fabricated by anchoring trace amounts of iridium onto dendritic gold (Au-D) *via* copper underpotential deposition and subsequent redox replacement. Structural, compositional, and electrochemical analyses revealed that Ir atoms were atomically dispersed on the Au-D surface, forming a high density of Ir/Au interfacial sites that synergistically enhanced OER activity.

The Ir/Au-D catalyst exhibited an impressive performance, including a low overpotential ( $\eta_{10} = 301$  mV), a small Tafel slope (36 mV  $\text{dec}^{-1}$ ), and a high turnover frequency ( $\text{TOF} = 3.03$   $\text{s}^{-1}$ ), outperforming benchmark Ir-based electrodes. Additionally, the catalyst demonstrated excellent long-term operational stability over 20 hours of continuous electrolysis.

Importantly, *in situ* surface-enhanced Raman spectroscopy (SERS) analysis confirmed the formation of  $\text{IrO}_x$  species and dynamic intermediates (*e.g.*,  $\mu$ -oxo bridges and O–O stretches) under operating conditions, providing direct evidence of Ir sites as the active centers for OER. These observations support the proposed mechanism involving interfacial charge redistribution and intermediate stabilization.

Taken together, these results highlight the effectiveness of combining ultrasmall noble metal loading with high-surface-area Au scaffolds and plasmonic monitoring capabilities to boost catalytic activity and durability. The Ir/Au-D system represents a promising platform for the design of next-generation low-metal-content oxygen evolution catalysts for energy conversion applications.

## Author contributions

Y. Lai conceived the project and designed the experiments. C. Tsai, and Y. Wang performed material preparation, structural characterization and electrochemical measurements. Y. Lai and C. Tsai analyzed the data. Y. Lai wrote the paper. All authors discussed the results and commented on the manuscript.

## Conflicts of interest

The authors declare no competing financial interest.

## Data availability

The data supporting this article have been included as part of the ESI.† The production model applied in this work is mainly based on the model of Degen *et al.*, which can be found under “Source Data Fig. 3” at <https://doi.org/10.1038/s41560-023-01355-z>.

## Acknowledgements

This work has been financially supported by the Ministry of Science and Technology of Taiwan (NSTC 113-2113-M-029-010, NSCT 113-2218-E-029-001 and NSTC 112-2113-M-029-001) and Tunghai University.

## References

- 1 N.-T. Suen, S.-F. Hung, Q. Quan, N. Zhang, Y.-J. Xu and H. M. Chen, *Chem. Soc. Rev.*, 2017, **46**, 337–365.
- 2 J. N. Hansen, H. Prats, K. K. Toudahl, N. Mørch Secher, K. Chan, J. Kibsgaard and I. Chorkendorff, *ACS Energy Lett.*, 2021, **6**, 1175–1180.
- 3 F.-H. Cho, M.-H. Huang, Y.-M. Chen, Y.-B. Huang, C.-J. Su, U. S. Jeng and Y.-H. Lai, *Appl. Surf. Sci.*, 2019, **485**, 476–483.
- 4 D. N. Oko, J. Zhang, S. Garbarino, M. Chaker, D. Ma, A. C. Tavares and D. Guay, *J. Power Sources*, 2014, **248**, 273–282.
- 5 Y. Wang, S. Tao, H. Lin, G. Wang, K. Zhao, R. Cai, K. Tao, C. Zhang, M. Sun, J. Hu, B. Huang and S. Yang, *Nano Energy*, 2021, **81**, 105606.
- 6 R. Subbaraman, D. Tripkovic, D. Strmcnik, K.-C. Chang, M. Uchimura, A. P. Paulikas, V. Stamenkovic and N. M. Markovic, *Science*, 2011, **334**, 1256–1260.
- 7 P.-C. Chen, M. Li, J. Jin, S. Yu, S. Chen, C. Chen, M. Salmeron and P. Yang, *ACS Mater. Lett.*, 2021, **3**, 1440–1447.
- 8 H. Okamoto and T. Massalski, *Materials Park*, ASM International, OH, USA, 1990, vol. 12, pp. 3528–3531.
- 9 B. S. Yeo and A. T. Bell, *J. Am. Chem. Soc.*, 2011, **133**, 5587–5593.
- 10 H.-C. Chen, C.-H. Chen, C.-S. Hsu, T.-L. Chen, M.-Y. Liao, C.-C. Wang, C.-F. Tsai and H. M. Chen, *ACS Omega*, 2018, **3**, 16576–16584.
- 11 Y.-H. Lai, S.-R. Li, H.-T. Chang, Y.-B. Huang, Y.-K. Li, Y.-M. Chen, S. B. Patil, S.-Y. Chang, P.-K. Chen and C.-C. Chang, *J. Mater. Chem. A*, 2021, **9**, 22901–22912.
- 12 F.-H. Cho, M.-H. Huang, Y.-M. Chen, Y.-B. Huang, C.-J. Su, U.-S. Jeng and Y.-H. Lai, *Appl. Surf. Sci.*, 2019, **485**, 476–483.
- 13 C. F. Crago, S. Li, A. M. Aleman, T. Siboonruang, M. Rojas Mendoza, T. F. Jaramillo and M. B. Stevens, *J. Am. Chem. Soc.*, 2025, **147**, 3925–3930.



- 14 C. Cai, S. Han, X. Zhang, J. Yu, X. Xiang, J. Yang, L. Qiao, X. Zu, Y. Chen and S. Li, *RSC Adv.*, 2022, **12**, 6205–6213.
- 15 X. Xu, C. Liu, P. Jiang, S.-H. Choi and T. Yu, *Dalton Trans.*, 2024, **53**, 11133–11140.
- 16 J. Suntivich, K. J. May, H. A. Gasteiger, J. B. Goodenough and Y. Shao-Horn, *Science*, 2011, **334**, 1383–1385.
- 17 U.-S. Jeng, C.-J. Su, K.-F. Liao, W.-T. Chuang, Y.-H. Lai, J.-W. Chang, Y.-J. Chen, Y.-S. Huang and M.-T. Lee, *Appl. Crystallogr.*, 2010, **43**, 110–121.
- 18 O. Shih, K.-F. Liao, Y.-Q. Yeh, C.-J. Su, C.-A. Wang, J.-W. Chang, W.-R. Wu, C.-C. Liang, C.-Y. Lin, T.-H. Lee, C.-H. Chang, L.-C. Chiang, C.-F. Chang, D.-G. Liu, M.-H. Lee, C.-Y. Liu, T.-W. Hsu, B. Mansel, M.-C. Ho, C.-Y. Shu, F. Lee, E. Yen, T.-C. Lin and U. Jeng, *J. Appl. Crystallogr.*, 2022, **55**, 340–352.
- 19 C.-Y. Chang, Y.-C. Hsieh, Y.-Y. Huang, Y.-J. Wang, Y.-M. Chen, Y.-B. Huang, W.-H. Hung and Y.-H. Lai, *J. Raman Spectrosc.*, 2019, **50**, 818–825.
- 20 Y.-B. Huang, Y.-K. Li, S. B. Patil, D.-Y. Wang, U.-S. Jeng and Y.-H. Lai, *ACS Appl. Energy Mater.*, 2025, DOI: [10.1021/acsaem.5c01299](https://doi.org/10.1021/acsaem.5c01299).
- 21 M. Fayette, Y. Liu, D. Bertrand, J. Nutariya, N. Vasiljevic and N. Dimitrov, *Langmuir*, 2011, **27**, 5650–5658.
- 22 Y.-G. Kim, J. Y. Kim, D. Vairavapandian and J. L. Stickney, *J. Phys. Chem. B*, 2006, **110**, 17998–18006.
- 23 F.-H. Cho, Y.-C. Lin and Y.-H. Lai, *Appl. Surf. Sci.*, 2017, **402**, 147–153.
- 24 Y.-H. Lai, S.-R. Li, H.-T. Chang, Y.-B. Huang, Y.-K. Li, Y.-M. Chen, S. B. Patil, S.-Y. Chang, P.-K. Chen, C.-C. Chang, Y.-C. Chen, C.-W. Pao, J.-L. Chen, C.-Y. Wei, I. K. Lin, H.-L. Chou, C.-J. Su, U. S. Jeng, T.-R. Kuo, C.-Y. Wen and D.-Y. Wang, *J. Mater. Chem. A*, 2021, **9**, 22901–22912.
- 25 J. Perez, E. R. Gonzalez and H. M. Villullas, *J. Phys. Chem. B*, 1998, **102**, 10931–10935.
- 26 N. D. Nikolić, J. D. Lović, V. M. Maksimović and P. M. Živković, *Metals*, 2022, **12**, 1201.
- 27 M. Lee, R. Arras, R. Takahashi, B. Warot-Fonrose, H. Daimon, M.-J. Casanove and M. Lippmaa, *ACS Omega*, 2018, **3**, 2169–2173.
- 28 Y. J. Park, J. Lee, Y. S. Park, J. Yang, M. J. Jang, J. Jeong, S. Choe, J. W. Lee, J.-D. Kwon and S. M. Choi, *Front. Chem.*, 2020, **8**, 593272.
- 29 C. Wang, A. Schechter and L. Feng, *Nano Res. Energy*, 2023, **2**, e9120056.
- 30 J. Cheng, J. Yang, S. Kitano, G. Juhasz, M. Higashi, M. Sadakiyo, K. Kato, S. Yoshioka, T. Sugiyama, M. Yamauchi and N. Nakashima, *ACS Catal.*, 2019, **9**, 6974–6986.
- 31 L. Trotochaud, J. K. Ranney, K. N. Williams and S. W. Boettcher, *J. Am. Chem. Soc.*, 2012, **134**, 17253–17261.
- 32 Y. Chen, J. Meng, M. Xu, L. Qiao, D. Liu, Y. Kong, X. Hu, Q. Liu, M. Chen, S. Lyu, R. Tong and H. Pan, *Adv. Funct. Mater.*, 2025, **35**, 2413474.
- 33 J. Guan, D. Li, R. Si, S. Miao, F. Zhang and C. Li, *ACS Catal.*, 2017, **7**, 5983–5986.
- 34 G. A. Kamat, J. A. Zamora Zeledón, G. T. K. K. Gunasooriya, S. M. Dull, J. T. Perryman, J. K. Nørskov, M. B. Stevens and T. F. Jaramillo, *Commun. Chem.*, 2022, **5**, 20.
- 35 K. H. Saeed, M. Förster, J.-F. Li, L. J. Hardwick and A. J. Cowan, *Chem. Commun.*, 2020, **56**, 1129–1132.
- 36 Z. Pavlovic, C. Ranjan, M. van Gastel and R. Schlögl, *Chem. Commun.*, 2017, **53**, 12414–12417.

